Plasmonics (2025) 20:4379–4392
https://doi.org/10.1007/s11468-024-02460-9

RESEARCH

Eccentric Core Photonic Crystal Fiber Magnetic Field Sensor Based on Surface Plasmon Resonance with Extremely High Linearity

Xingdi Luo[1] · Jingwei Lv[1] · Wei Liu[1] · Chao Mi[3] · Jianxin Wang[1] · Xili Lu[2] · Lin Yang[1] · Qiang Liu[1] · Paul K. Chu[4] · Chao Liu[1]

Received: 1 July 2024 / Accepted: 24 July 2024 / Published online: 5 November 2024

Abstract

A micro-polished eccentric core photonic crystal fiber magnetic field sensor based on surface plasmon resonance (PCF-SPR) with a ring-shaped opening is designed. In the sensor, metal nanowires are placed inside the ring-shaped opening to excite SPR to replace the traditional coating process and enhance the sensing stability. Aluminum and gold are assessed as the SPR materials. When Al is the plasmonic medium, the sensor has a wider detection range and higher figure of merit (FOM), but the linearity of the resonant wavelength (RW) is not satisfactory. On the other hand, when Au is the plasmonic medium, the sensor shows excellent magnetic field sensitivity and resolution, in addition to ultra-high linearity in the RW, making it more suitable for magnetic field detection. The structural parameters are optimized, and the effects of different metals and temperatures on the sensing properties are investigated numerically. The sensor with Al shows a detection range of 40–200 Oe, maximum magnetic field sensitivity of 3000 pm/mT, and R^2 of 0.99988, whereas the Au sensor exhibits a detection range of 40–150 Oe, maximum magnetic field sensitivity of 9000 pm/mT, and RW R^2 of 0.99995. The PCF-SPR magnetic field sensor boasts a simple structure, wide detection range, high sensitivity, and good linearity. It has broad application prospects in mineral resource exploration, seismic and tsunami monitoring, medical diagnostics, and other fields.

Keywords Magnetic field sensor · Magnetic fluid · Surface plasmon resonance · Magnetic field sensitivity · High linearity

Introduction

Surface plasmon resonance (SPR) refers to the phenomenon of resonance of free electrons on the surface of a metal under the action of an external electric field [1]. When the momenta of photons and free electrons are consistent, the free electrons in the metal absorb the energy of incident light at the metal–dielectric interface to generate collective oscillations [2]. SPR sensing has attracted a lot of attention due to the simple detection process, real-time dynamic monitoring, and label-free detection. Accurate monitoring of the magnetic field is crucial to the aerospace, biomedical, seismic monitoring, and other industries. Magnetic field sensors based on the principle of SPR have become a research hotspot because of their strong anti-interference ability, high sensitivity, and high linearity [3].

The photonic crystal fiber (PCF) is a type of optical fiber [1] possessing unique characteristics such as small size, flexible design, remote controllability, and compact, smooth structure [2] and can be incorporated into magnetic field sensors based on SPR. Common optical fiber magnetic field sensors mainly utilize the Faraday rotation effect and magnetostrictive properties [4, 5]. However, they suffer from drawbacks like complex signal demodulation, low sensitivity, and limited magnetic field detection range. In contrast, optical fiber magnetic field sensors composed of magnetic fluids (MF) exhibit advantages such as magnetically controllable refractive index and high

✉ Chao Liu
msm-liu@126.com

1 School of Physics and Electronic Engineering, Northeast Petroleum University, Daqing 163318, China

2 School of Materials Science and Chemical Engineering, Harbin Engineering University, Harbin 150001, China

3 Digital Intelligence Technology Company, Daqing Oilfield, Daqing 163453, China

4 Department of Physics, Department of Materials Science and Engineering, and Department of Biomedical Engineering, City University of Hong Kong, Tat Chee Avenue, Kowloon, Hong Kong, China

magnetic field sensitivity [6, 7]. Hence, there is increasing interest in magnetic sensors based on MF.

Wang et al. have proposed a d-type PCF-SPR sensor [8]. By depositing a gold film inside a large-diameter air hole and filling the hole with MF, the maximum magnetic field sensitivity is 779 pm/mT with an R^2 of 0.9937 in the magnetic field range of 25–200 Oe. Wang et al. have designed a dual-parameter sensor based on PCF-SPR for the detection of magnetic field and temperature [9]. Two elliptical channels are incorporated on both sides of the fiber core with a gold film deposited and an MF-filled left channel. The sensor can detect magnetic fields in the range of 50–130 Oe, with a maximum magnetic field sensitivity of 650 pm/mT. However, depositing a metal film inside air holes raises the manufacturing complexity and cost [6].

Tang et al. have proposed a PCF-SPR sensor with high magnetic field sensitivity comprising a hexagonal regular arrangement [10]. Magnetic field detection is achieved by injecting MF into the two large air holes with a diameter of 2 μm. The magnetic field detection range is 30–150 Oe, with a maximum magnetic field sensitivity of 1150 pm/Oe and an *R*-square value of only 0.98266. Although the sensitivity of the PCF-SPR magnetic field sensor has been improved, its linearity is still quite poor. Additionally, filling the MF into specified holes while ensuring the absence of analytes in other air holes presents significant challenges. Moreover, the coating may be uneven and prone to detachment, resulting in poor sensing linearity. Therefore, the design of a magnetic field sensor with high sensitivity, simple structure, no need to fill analytes, and ultra-high linearity is highly desirable but challenging.

In this study, a biased-core PCF-SPR magnetic field sensor with a micro-polished ring opening is designed and presented. The structure of this sensor is very simple, and the cladding consists of only air holes of one size to facilitate manufacturing. The sensor is constructed by placing metal nanowires inside the ring opening and then placing the sensor into hydrated Fe_3O_4 MF. This process avoids the difficulty of air holes with the analyte. The effects of air hole diameter, air hole spacing, metal nanowire diameter, and metal type on the sensing properties are investigated by the finite element method. The characteristics of the magnetic field sensors with Al nanowires and Au nanowires as the plasmonic media are determined. The eccentric core photonic crystal fiber magnetic field sensor proposed in this article shortens the distance from the fiber core to the analyte [11]. Compared with traditional half-polished D-shaped fibers, this sensor only requires a slight polishing treatment to significantly reduce the distance between the metal nanowires and the fiber core, thus achieving effective coupling and higher sensitivity. The results show that the magnetic field sensor utilizing Al-excited SPR can detect magnetic fields in the range of 40–200 Oe with a maximum magnetic field sensitivity of 3000 pm/mT and R^2 of 0.99988. In comparison, the magnetic field sensor exploiting Au-excited SPR can detect magnetic fields in the range of 40–150 Oe, with a maximum magnetic field sensitivity of 9000 pm/mT, a minimum magnetic field sensitivity of 8500 pm/mT, and RW R^2 of 0.99995, which are higher than those of recently reported sensors [8, 10]. Between the two sensors, Au produces better properties such as linearity. Due to the simple structure, high sensitivity, good linearity, and easy manufacturing, the sensor has large potential in many applications such as geological exploration and biomedicine.

Model and Theory

The two-dimensional cross-section of the micro-polished eccentric PCF-SPR magnetic field sensor with a ring opening is depicted in Fig. 1b. Figure 1a shows the structure of the PCF before polishing, and the PCF is polished until the first air hole is exposed. The sensor structure is simple, with the PCF cladding consisting of air holes of only one size arranged hexagonally and equally spaced, consequently reducing the manufacturing complexity and cost. The metal nanowires are placed inside the annular opening to excite SPR to replace the traditional coating process and improve issues such as uneven coating thickness and delamination. The location with air holes (four) in the cladding is the core for light transmission. The annular opening decreases the distance between the sensing layer to the core to enhance the coupling effect between the fundamental mode and surface plasmon polariton (SPP) mode [11, 12]. The structural parameters D, Λ, and d represent the diameter of the air holes (D), the spacing between the air holes (Λ), and the diameter of the metal nanowires in the plasmonic material (d). The magnetic fluid is located outside the sensor, thus allowing magnetic field detection by placing the sensor in a magnetic fluid solution. In this way, the complicated operation of filling the magnetic fluid into specific air holes can be avoided [3]. A perfectly matched layer (PML) is established to improve the simulation accuracy [13]. The proposed eccentric core PCF magnetic field sensor can be manufactured using advanced stacking-drawing process and side polishing method [1]. The fabrication of the PCF preform only requires one type of silica capillary and solid silica rod, with the same outer diameter. Stack these capillaries and solid rods in the manner shown in Fig. 1c. By using the side polishing method, the PCF can be prepared with the designed structure. The proposed PCF-SPR magnetic field sensor was prepared by placing the metal nanowires prepared using the chemical vapor deposition method inside the openings of the PCF and fixing them at the end of the PCF using a small amount of curing agent.

The detection device for magnetic field strength is shown in Fig. 1d. The designed PCF-SPR magnetic field sensor is placed on a temperature-controlled platform at a constant temperature of 24.3 ℃. Single-mode optical fiber (SMF) is

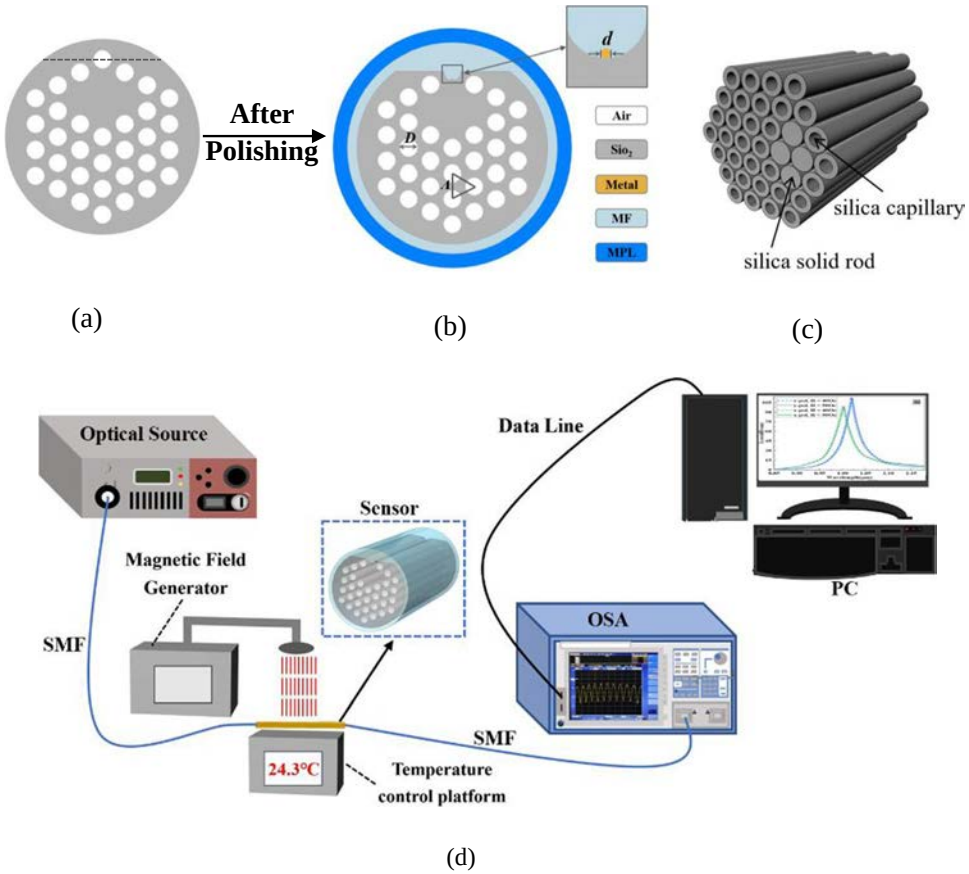

Fig. 1 **a** PCF structure before polishing. **b** PCF-SPR magnetic field sensor 2D cross-section. **c** Stacked prefabrication of PCF in 3D model. **d** Device diagram of PCF-SPR sensor to detect magnetic field intensity

connected to the sensor on both sides using a fiber fusion machine to ensure smooth transmission of light. One side of the SMF is connected to the light source, the other side is connected to the optical spectrum analyzer (OSA), and then, the OSA is connected to the computer using a data cable for real-time data transmission and processing. Finally, the light source and magnetic field generator are turned on, and the SPR is excited in the desired wavelength band to obtain the loss spectrum. The magnetic field strength is determined by analyzing the resonance wavelength in the loss spectrum.

Fused silica is the bulk material used for the sensor cladding. The refractive index of fused silica at different wavelengths is determined by the temperature-dependent Sellmeier Eq. (1) [14]:

$$n^2(w,T) = 1.31552 + A_1 T + \frac{4\pi^2 c^2 (B_1 + B_2 T)}{4\pi^2 c^2 - w^2 (B_3 + B_4 T)} + \frac{4\pi^2 c^2 (C_1 + C_2 T)}{4\pi^2 c^2 - 100 w^2}, \quad (1)$$

where $A_1 = 6.90754 \times 10^{-6}$, $B_1 = 0.788404$, $B_2 = 2.35835 \times 10^{-5}$, $B_3 = 0.0110199$, $B_4 = 0.584758 \times 10^{-6}$, $C_1 = 0.91316$, $C_2 = 0.548368 \times 10^{-6}$, c represents the speed of light, $c = 3 \times 10^8$ m/s, and T is the ambient temperature.

The plasmonic metal has a significant impact on the characteristics of the sensor. For common metals such as Au, Ag, Cu, and Al, their relative dielectric constants are calculated by the following Eq. (2) [15]:

$$\varepsilon(\lambda) = 1 \frac{\lambda^2 \lambda_c}{\lambda_p^2 (\lambda_c + i\lambda)} \quad (2)$$

where λ is the wavelength in micrometer; the values of λ_c and λ_p for different metals are shown in Table 1.

The magnet fluid (MF) is hydrated Fe_3O_4 with a concentration of 0.68 emu/g. The refractive index $n_{MF}(H, T)$ versus magnetic field and temperature is shown in Eq. (3) [16]:

$$n_{MF}(H,T) = (n_s - n_0) \left[\coth\left(\alpha \frac{H - H_{c,n}}{T} \right) - \frac{T}{\alpha (H - H_{c,n})} \right] + n_0, \quad (3)$$

where $n_0 = 1.4352$ is the initial refractive index, $n_s = 1.4383$, $\alpha = 5$ is the fitting coefficient, $H_{c,n} = 3$ mT is the critical magnetic field strength, T is the thermodynamic temperature, and H is the magnetic field strength [16]. Owing to the influence of the temperature, a temperature control device is needed to ensure the stability of the experimental environment and reduce errors caused by temperature fluctuations. The initial T is 297.45 K. When $H > H_{c,n}$, the refractive index of the MF starts to change with the external magnetic field. When 0 mT $\le H \le$ 3 mT or $H >$ 20 mT, the refractive index of the MF does not change. Therefore, the hydrated Fe_3O_4 MF can be used to detect a magnetic field of 3–20 mT.

Table 1 λ_c and λ_p of different metals

Metal	λ_c (μm)	λ_p (μm)
Ag	17.614	0.14541
Cu	40.852	0.13617
Al	24.511	0.10657

In this work, the core model confinement loss method is employed to investigate the sensing properties of the sensor. The confinement loss (CL) can be calculated by Eq. (4) [17]:

$$\mathrm{CL} = 8.686 \times \frac{2\pi}{\lambda} \mathrm{Im}\left[n_{\mathrm{eff}}\right] \times 10^4 (\mathrm{dB/cm}), \tag{4}$$

where λ is the wavelength in micrometer and $\mathrm{Im}[n_{\mathrm{eff}}]$ is the imaginary part of the effective refractive index.

The essence of SPR is the energy exchange between the fundamental mode and the surface plasmon polariton (SPP) mode [18], which can be characterized by the electric field distribution and refractive index change curve in Fig. 2. The effective refractive index real parts of the fundamental mode (black dashed line) and the SPP mode (blue dashed line) intersect at 1.0365 μm, while the CL of the fundamental mode reaches the maximum, satisfying the phase matching condition. The wavelength corresponding to the intersection point is defined as the resonance wavelength (RW). When the wavelength is less than RW, the effective refractive index real part of the SPP mode is greater than that of the fundamental mode, and the losses of the fundamental mode increase accordingly. At this time, the energy is mainly concentrated in the fiber core, and the electric field distributions of the fundamental and SPP modes are shown in Fig. 2a and c, respectively. When the wavelength is equal to RW, the real part of the effective refractive index of the two modes is equal [19], at which time the energy is maximally coupled from the inside of the fiber core to the surface of the metal nanowires giving rise to SPR.

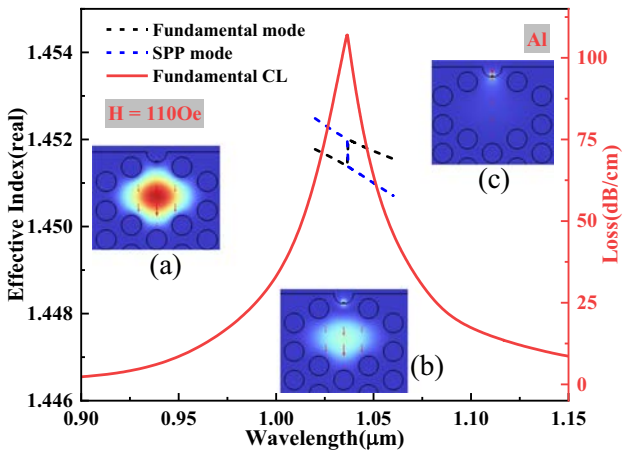

Fig. 2 Fundamental mode effective refractive index (black dashed line), SPP mode effective refractive index (blue dashed line), and fundamental mode loss (red curve) versus wavelength, with the inset showing the electric field distribution of 110 Oe

The electric field distribution is shown in Fig. 2b. When the wavelength is larger than RW, the repulsion between free electrons on the surface of the metal nanowires becomes stronger, and the energy is driven back to the fiber core. The real part of the effective refractive index of the SPP mode is thus smaller than that of the fundamental mode, and the fundamental mode loss decreases accordingly. Therefore, the combination of the relation curve and the electric field distribution elucidates the basic principle and significance of SPR.

The important properties of the PCF-SPR magnetic field sensor include the magnetic field sensitivity, resolution (R), and figure of merit (FOM). Here, wavelength modulation is used to analyze the spectral changes. When the magnetic field changes, the refractive index of the MF changes, and the RW is displaced. The magnetic field sensitivity of the sensor is obtained by calculating the displacement of RW by Eq. (5) [20]:

$$S_{\mathrm{m}} = \frac{\Delta\lambda_{\mathrm{peak}}}{\Delta H} (\mathrm{pm/mT}), \tag{5}$$

where $\Delta\lambda_{\mathrm{peak}}$ is the resonance wavelength change and ΔH is the applied magnetic field change. The higher the magnetic field sensitivity, the faster the sensor responds to changes in the magnetic field.

The resolution (R) is the ability of the sensor to measure the smallest change in the magnetic field, as shown in Eq. (6) [21]:

$$R = \frac{\Delta H \Delta\lambda_{\mathrm{min}}}{\Delta\lambda_{\mathrm{peak}}} (\mathrm{mT}), \tag{6}$$

where $\Delta\lambda_{\mathrm{min}}$ is the minimum measurable value of the spectrometer, generally 0.1 pm. A smaller R translates into a higher detection accuracy.

The figure of merit (FOM) reflects the comprehensive performance of the sensor. The larger the FOM, the better the sensing properties. It is calculated by Eq. (7) [22]:

$$\mathrm{FOM} = \frac{S_{\mathrm{m}}}{\mathrm{FWHM}} \left(\mathrm{mT}^{-1}\right), \tag{7}$$

where S_{m} is the magnetic field, and FWHM is the full-width at half-maximum of the loss curve. In order to better detect the magnetic field strength, the FOM should be maximized while ensuring high magnetic field sensitivity and low resolution.

Amplitude sensitivity is another important performance parameter of the sensor, which can be calculated by Eq. (8) [17].

$$\mathrm{AS} = \frac{1}{\alpha\left(\lambda, H_a\right)} \times \frac{\partial\alpha\left(\lambda, H_a\right)}{\partial H_a} \left(\mathrm{mT}^{-1}\right), \tag{8}$$

where $\partial\alpha(\lambda, H_{\mathrm{a}})$ represents the change between two adjacent loss spectra, $\alpha(\lambda, H_{\mathrm{a}})$ is the total loss, and ∂H_{a} is the change in adjacent magnetic field intensity.

Sensor Optimization

Selection of x- and y-Polarization Modes

Owing to the asymmetry of the sensor, both *x*-polarized and *y*-polarized fundamental modes are present in this structure. Figure 3a shows the CL curves of the two polarization modes for magnetic field strengths of 40 Oe and 50 Oe. The CL peaks are larger for *y*-polarization, indicative of better mode coupling and more energy coupling between the fiber core and metal nanowires. The magnetic field sensitivity is 3000 pm/mT for both polarization modes. The *x*-polarization mode has a FOM of 7.99×10^{-2} mT^{-1}, and that of the *y*-polarization is 8.98×10^{-2} mT^{-1}. The *y*-polarization mode has a larger FOM for the same sensitivity and is chosen for our subsequent analysis.

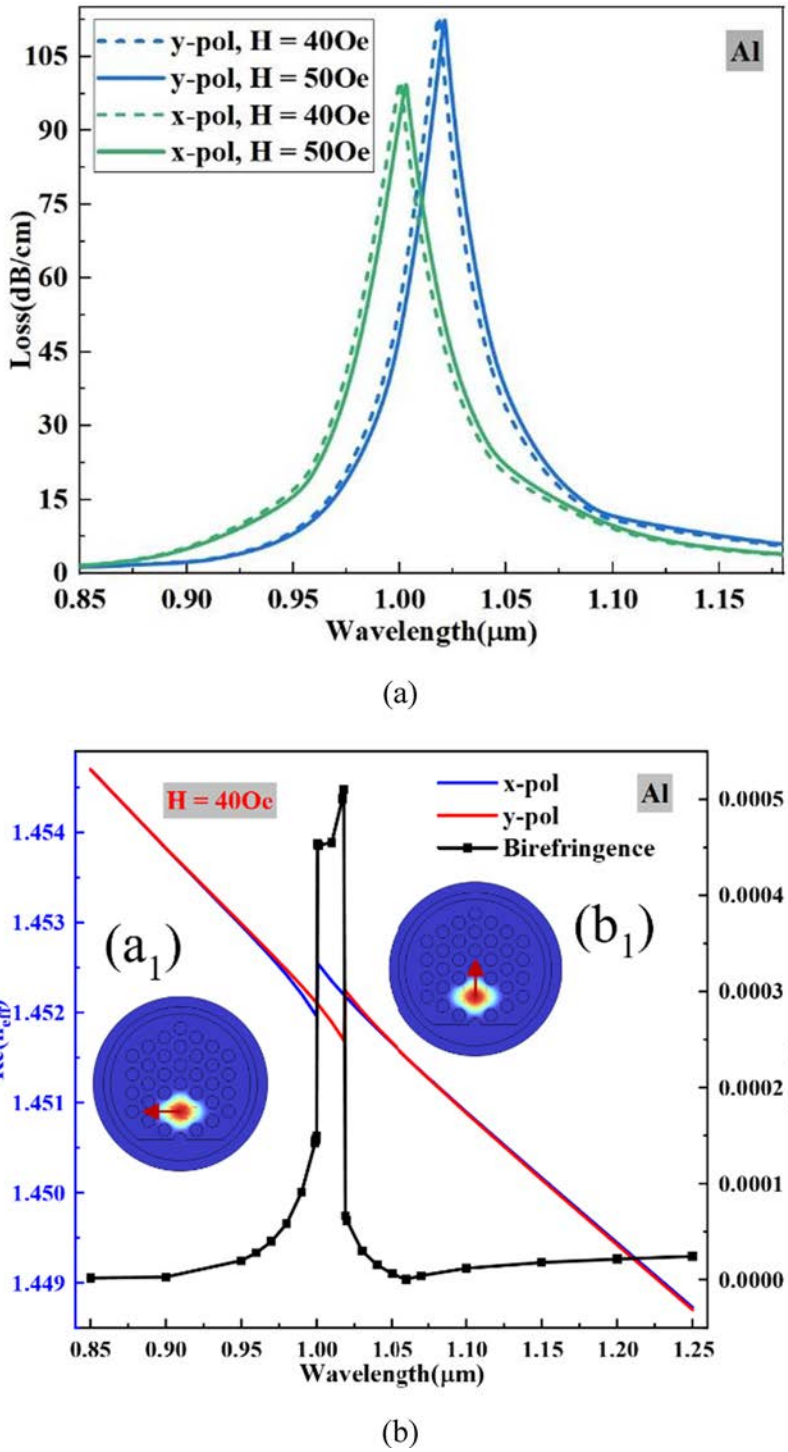

Fig. 3 **a** CL for *x*-polarization and *y*-polarization. **b** The birefringence curves for two polarizations and the real part of the effective refractive index, with (a_1) and (b_1) displaying the electric field distribution for the *x*-polarized mode and *y*-polarized mode, respectively

In addition, the birefringence of the sensor can be analyzed by two polarizations, *x*-polarization and *y*-polarization; birefringence is an important indicator for evaluating sensors. High birefringence helps maintain the polarization state of the input signal and enhances the overall stability of optical operations [11]. The birefringence of a sensor can be calculated using Eq. (9) [11].

$$B = \left| n_x - n_y \right|, \tag{9}$$

where n_x and n_y are the effective refractive index real parts of the *x*-polarization mode and *y*-polarization mode respectively. Figure 3b shows the birefringence curve and the effective refractive index real parts of the two polarization modes at an applied field strength of $H = 40$ Oe. It can be seen from the graph that a strong birefringence response of 5.1×10^{-4} is obtained at the resonance wavelength of 1018 nm for the *y*-polarization, indicating that the sensor has strong overall stability in optical operations. The electric field distributions for the *x*-polarization and *y*-polarization are shown in the insets (a_1) and (b_1) of Fig. 3b, respectively.

Optimization of Structural Parameters

The structural parameters of the sensor have a profound impact on the optical characteristics of the sensor [17]. Figure 4a shows the CL curves for different values of *D*. As *D* increases between 3.2 and 4.0 μm, the RW blueshifts because the refractive index of the fiber core increases and the phase velocity decreases. According to Fig. 3d, when *D* is 3.6 μm, the sensor has the magnetic field sensitivity and FOM, and therefore, the optimal *D* is determined to be 3.6 μm.

Figure 4b shows the CL curves for different values of ∧. As ∧ increases from 5.0 to 5.5 μm, the RW shows a blueshifting trend because of the gradual increase of the refractive index of the fiber core. According to Fig. 4e, when ∧ is 5.25 μm, the sensor has the highest magnetic field sensitivity and maximum FOM. Hence, the optimal value of ∧ is determined to be 5.25 μm.

Figure 4c shows the optimization of the Au nanowire diameter. The CL curves for different values of *d* are

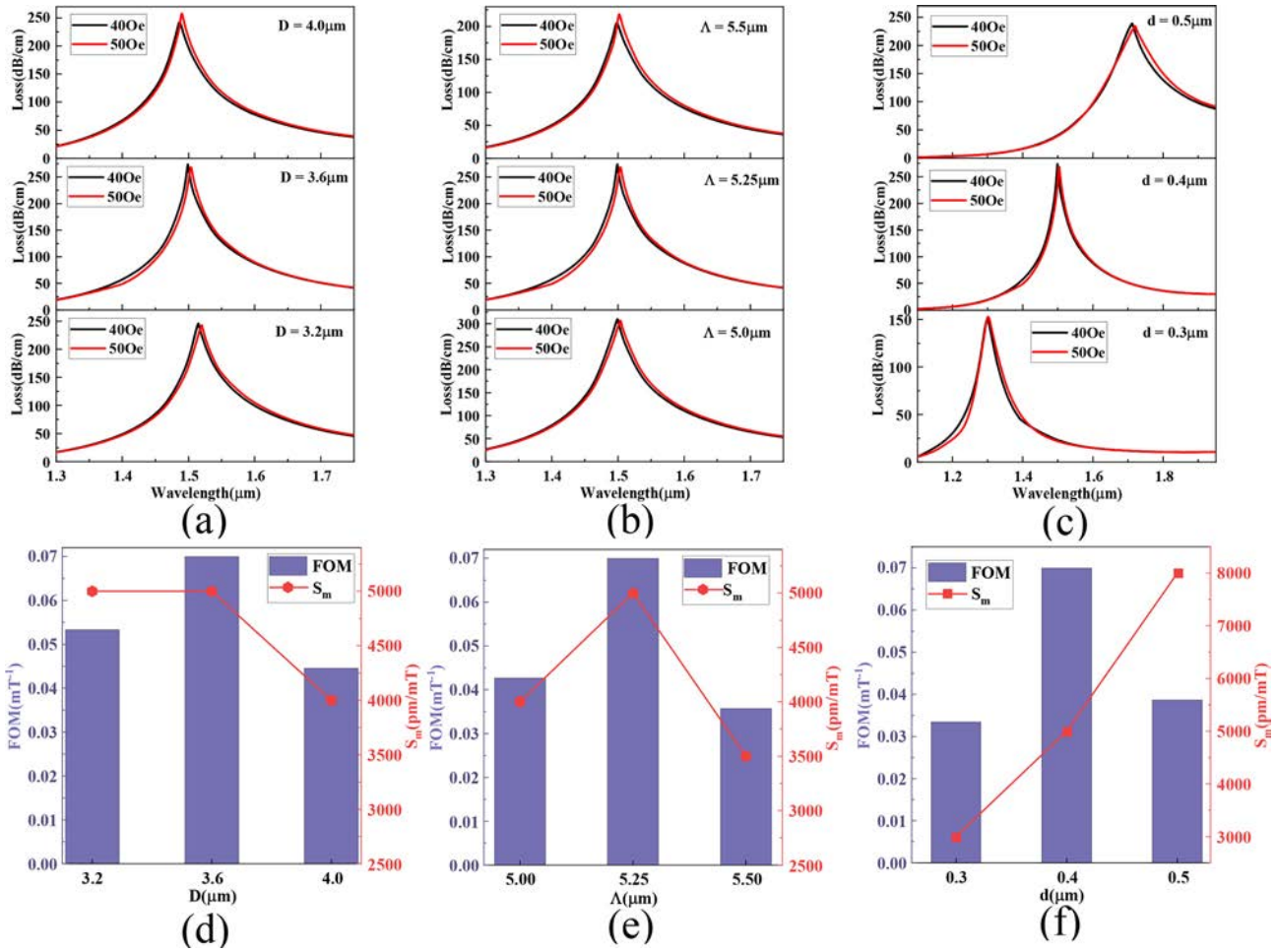

Fig. 4 Fundamental mode loss: **a** different *D*; **b** different ∧; **c** different *d*. Magnetic field sensitivity and FOM of the PCF-SPR magnetic field sensor: **d** different *D*; **e** different ∧; **f** different *d*

shown in Fig. 4c. As d increases from 0.3 to 0.5 μm, the RW shows a redshifting trend because more photon energy is coupled from the fiber core to the nanowires, thereby decreasing the refractive index of the fiber core, increasing the phase velocity, and causing redshifting of the loss peak. According to Fig. 4f, when d is 0.4 μm, the FOM is maximum, and when d is 0.5 μm, the magnetic field sensitivity is maximum.

Metal Optimization

The plasmonic metal impacts the properties of the magnetic field sensor. For common metals like Au, Ag, Cu, and Al [23], the relative permittivity can be determined by Eq. (2).

Figure 5a shows the CL curves of the fundamental mode for the four different metals at 40 Oe and 50 Oe.

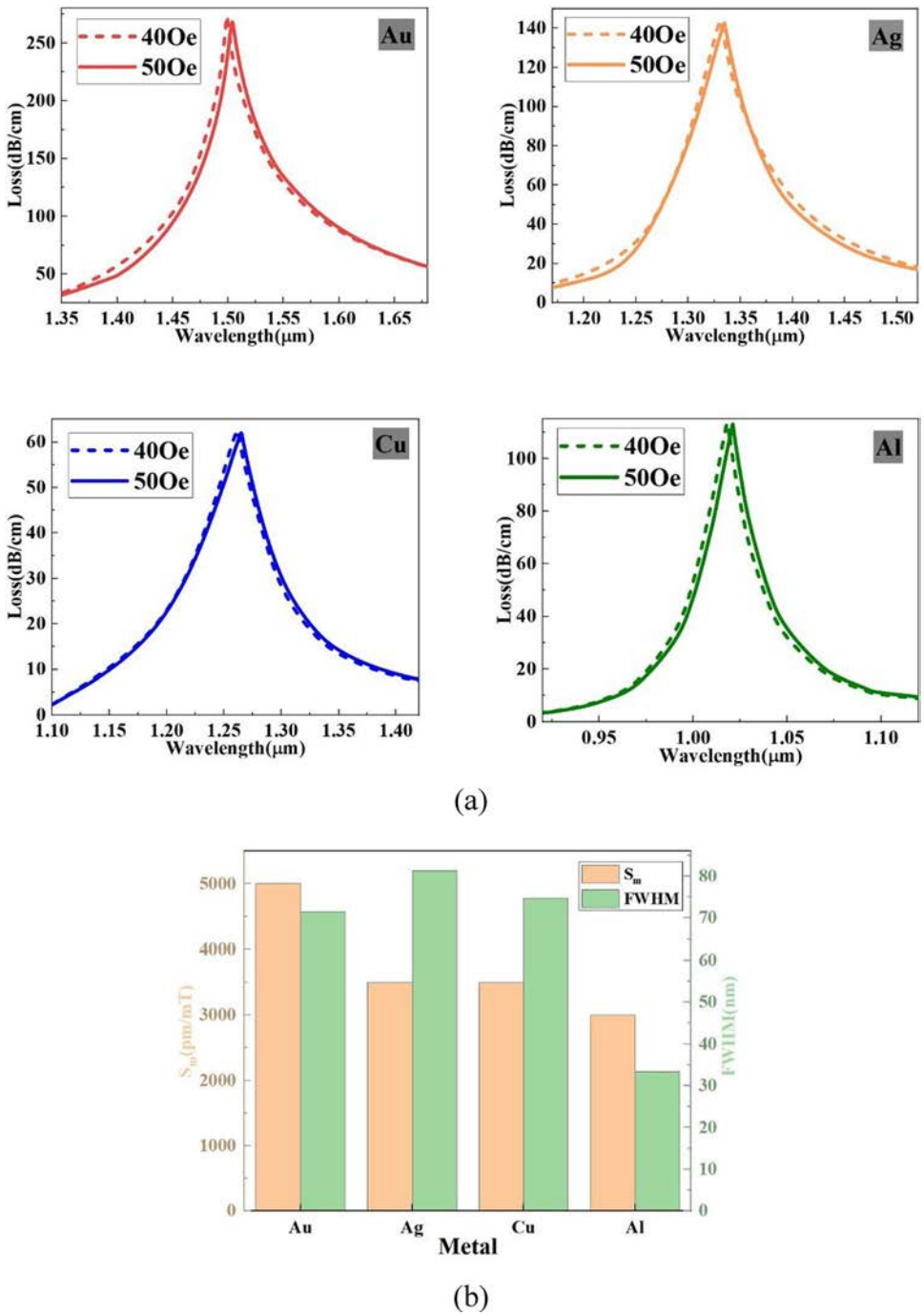

Fig. 5 **a** Fundamental mode loss for different metals. **b** FWHM and magnetic field sensitivity for different metals

Although all four metals can excite SPR, the magnetic field sensitivity and FWHM vary. Figure 5a shows that when Al is used, the loss peak is sharper, indicating successful phase matching between the fundamental mode and SPP mode as well as better coupling effects. According to Fig. 5b, the sensor with Al has the smallest FWHM and largest FOM. When Au is used, the sensor shows the highest magnetic field sensitivity. The optimal structural parameters of the magnetic field sensor with Al-excited SPR are evaluated in terms of the FOM, and the optimal parameters D, $\wedge$, and d are 3.6 μm, 5.25 μm, and 0.4 μm, respectively. As for the magnetic field sensor with Au in terms of the magnetic field sensitivity, the optimal parameters D, $\wedge$, and d are 3.6 μm, 5.25 μm, and 0.5 μm, respectively.

Results and Discussion

Figure 6a shows the CL curves of the PCF-SPR magnetic field sensor under different external magnetic field strengths for Al. Figure 6a shows that as the magnetic field strength increases, the RW redshifts because the refractive index of the MF increases [16], leading to more energy transferred from the core to the metal nanowires [2]. This reduces the effective refractive index of the fundamental mode, increases the phase velocity, and ultimately causes the loss peak to redshift. Figure 6b shows the peak loss and magnetic field sensitivity for different magnetic field strengths. Figure 6a and b shows that as the external magnetic field strength increases, the peak loss decreases. The peak loss of the fundamental mode is below 113.68 dB/cm, with a minimum value of 102.07 dB/

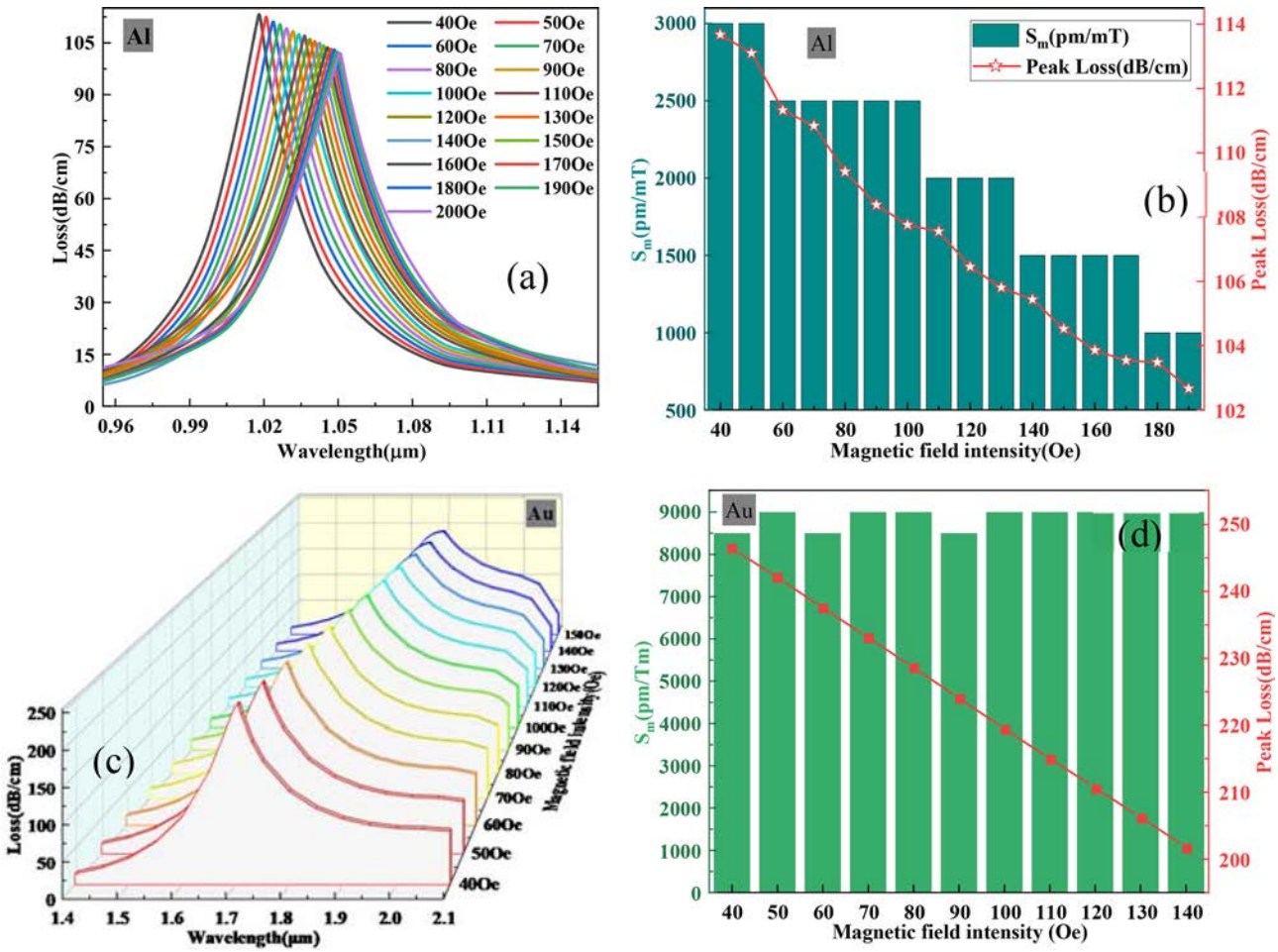

Fig. 6 Fundamental mode loss curves for different magnetic field strengths: **a** excited SPR using Al; **c** excited SPR using Au. Magnetic sensitivity and peak loss for different magnetic field strengths: **b** excited SPR using Al and **d** excited SPR using Au

cm ($H=200$ Oe). This sensor can detect magnetic fields in the range of 40 to 200 Oe. When $H=40$ Oe, the magnetic field sensitivity is the highest at 3000 pm/mT.

Figure 6c shows the CL curves of the PCF-SPR magnetic field sensor under different external magnetic field strengths when Au is used. Figure 6c shows that as the magnetic field strength increases, the RW redshifts. The reason is the same as that observed from Al.

Figure 6d shows the peak loss and magnetic field sensitivity for different magnetic field strengths. Figure 6c and d shows that as the external magnetic field increases, the peak loss decreases linearly. This sensor can detect magnetic fields in the range of 40 to 150 Oe. In this range, the maximum magnetic field sensitivity is 9000 pm/mT, the minimum magnetic field sensitivity is 8500 pm/mT, and the average magnetic field sensitivity is 8863.64 pm/mT. The results indicate that the sensitivity of the magnetic field sensor consisting of Au is stable and it favors magnetic field detection.

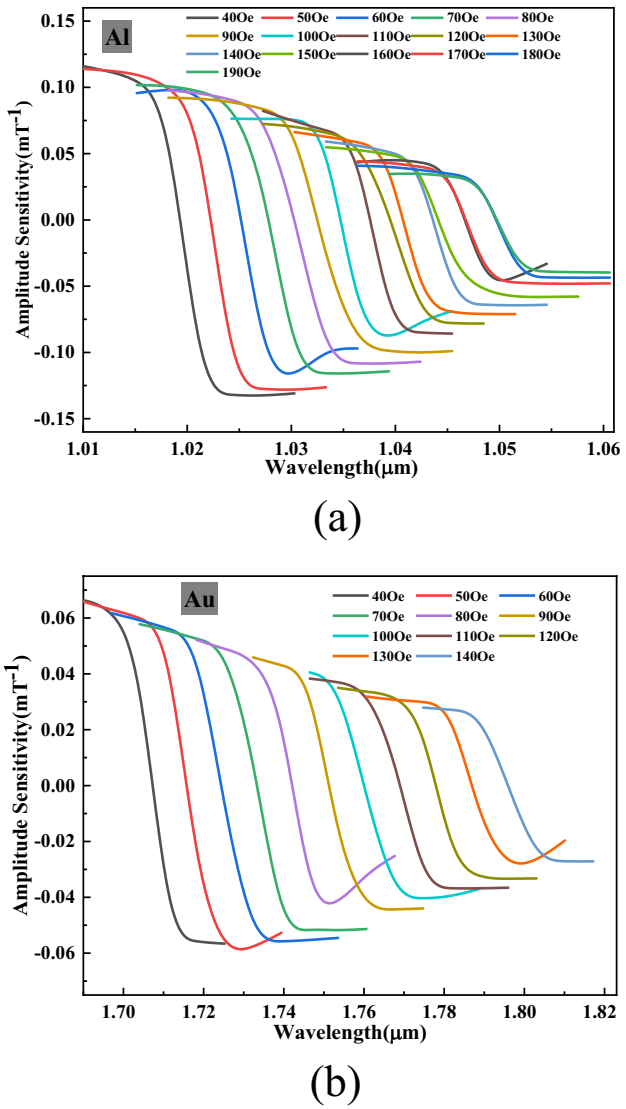

Fig. 7 Amplitude sensitivity at different magnetic field intensities: **a** sensors with Al-excited SPR; **b** sensors with Au-excited SPR

Figure 7a and b respectively describe the relationship between amplitude sensitivity and operating wavelength at different magnetic field strengths when exciting SPR using Al and Au. It can be observed from the figures that when exciting SPR using Al or Au, the sensor has the highest amplitude sensitivity at a magnetic field intensity of 40Oe, with values of -0.133 mT^{-1} and -0.061 mT^{-1}, respectively.

Figure 8a and b show the R and RW of the magnetic field sensor, respectively, when SPR is excited from Al. Figure 8a shows that R increases gradually with the magnetic field, showing the optimal R of 3.33×10^{-5}mT when $H=40$ Oe. Figure 8b shows the RW of the sensor and the fitted curve shown in Eq. (10):

$$Y_1 = 1.005 + \mathrm{AH} - \mathrm{BH}^2 - \mathrm{CH}^3 \ (40\ \mathrm{Oe} \le H \le 200\ \mathrm{Oe}), \quad (10)$$

where $A=3.321\times10^{-4}$, $B=3.838\times10^{-7}$, $C=7.525\times10^{-10}$, and $R^2=0.99988$.

Figure 8c and d show the R and RW of the magnetic field sensor, respectively, when SPR is excited by Au. Figure 8c shows that the change in the magnetic field strength has almost no effect on R, with a minimum R of 1.11×10^{-5}mT and a maximum of 1.18×10^{-5}mT. Figure 8d shows the RW of the sensor and the linear fit expressed by Eq. (11):

$$Y_2 = 1.667 + 8.871\times10^{-4}\ H \ (40\ \mathrm{Oe} \le H \le 150\ \mathrm{Oe}), \quad (11)$$

For magnetic field sensors, when the RW shows a high linearity, it can more accurately predict RW within a specific range of the magnetic field strengths. The linearity of the sensor RW is very good, with an R^2 up to 0.99995 based on the linear fitting with a first-order function, which surpasses those reported in the recent literature [8, 10, 16]. This confirms the accuracy and reliability of the sensor.

The changes in FWHM and FOM as a function of magnetic field strength are shown in Fig. 9, which shows that the FWHM is directly proportional to magnetic field strength, while FOM is inversely proportional to magnetic field strength. Figure 9a displays the FWHM and FOM of different magnetic field strengths for SPR excited by Al. It is evident that with increasing magnetic field strength,

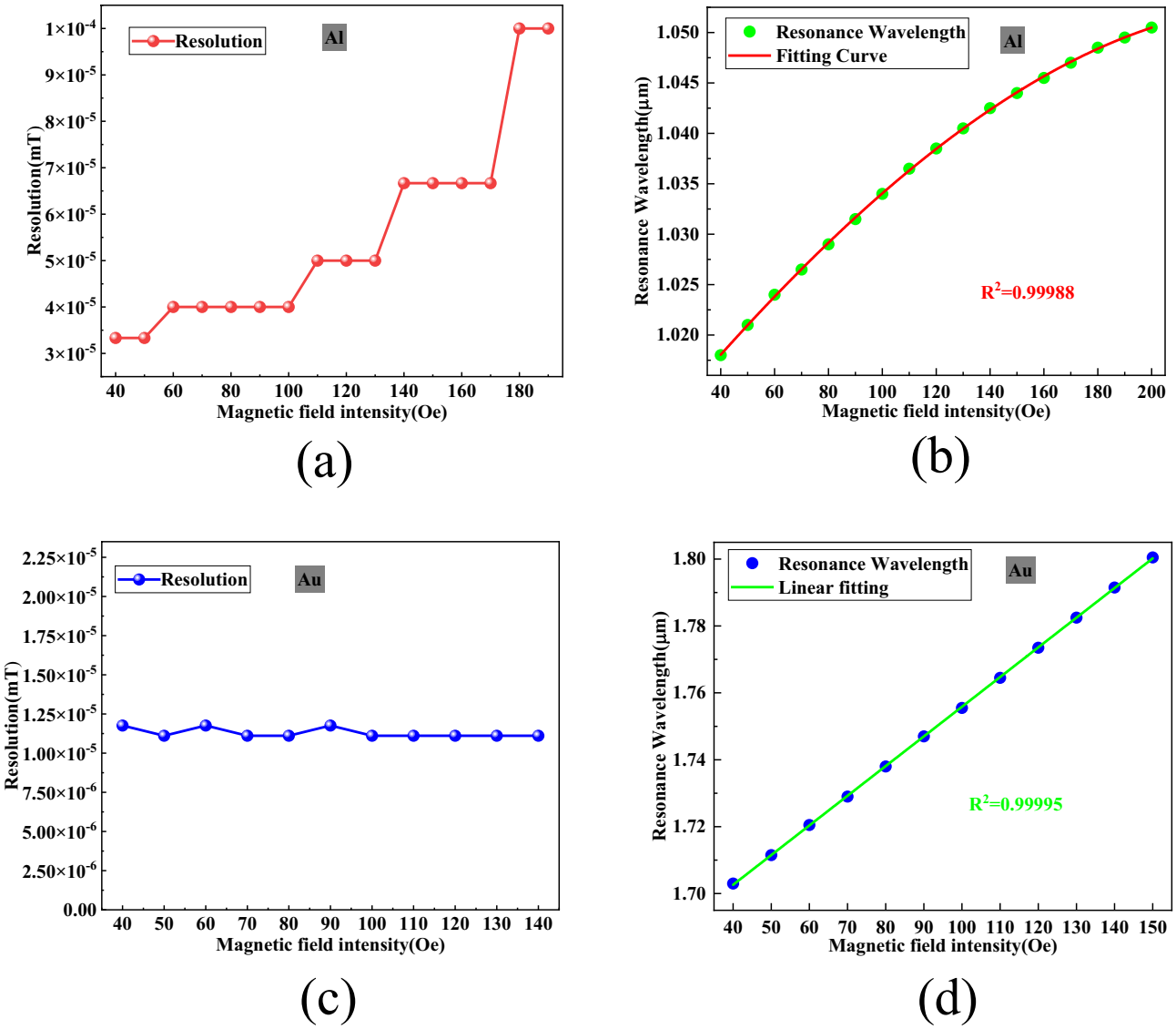

Fig. 8 Resolution for different magnetic field strengths: **a** SPR excited by Al and **c** SPR excited by Au; resonance wavelengths for different magnetic field strengths and linear fitting: **b** SPR excited by Al and **d** SPR excited by Au

FWHM increases but FOM decreases. At $H = 40$ Oe, the maximum FOM is 0.09 mT^{-1}. Figure 9b shows the FWHM and FOM of different magnetic field strengths for Au. At $H = 40$ Oe, the maximum FOM is 0.046 mT^{-1}. In conclusion, although the FOM of the magnetic field sensor using Au to excite SPR is slightly smaller than that of the sensor using Al, the former exhibits superior magnetic field sensitivity and resolution. Of particular importance is its high linearity of RW, thus ensuring the stability of the sensor and facilitating magnetic field detection.

Signal-to-noise ratio (SNR) and detection limit (DL) are also considered important performance parameters [24]. SNR is used to measure the ratio of signal to noise, with higher SNR indicating better performance of the sensor. DL represents the lowest amount of analyte that the proposed sensor can accurately detect, with smaller values being

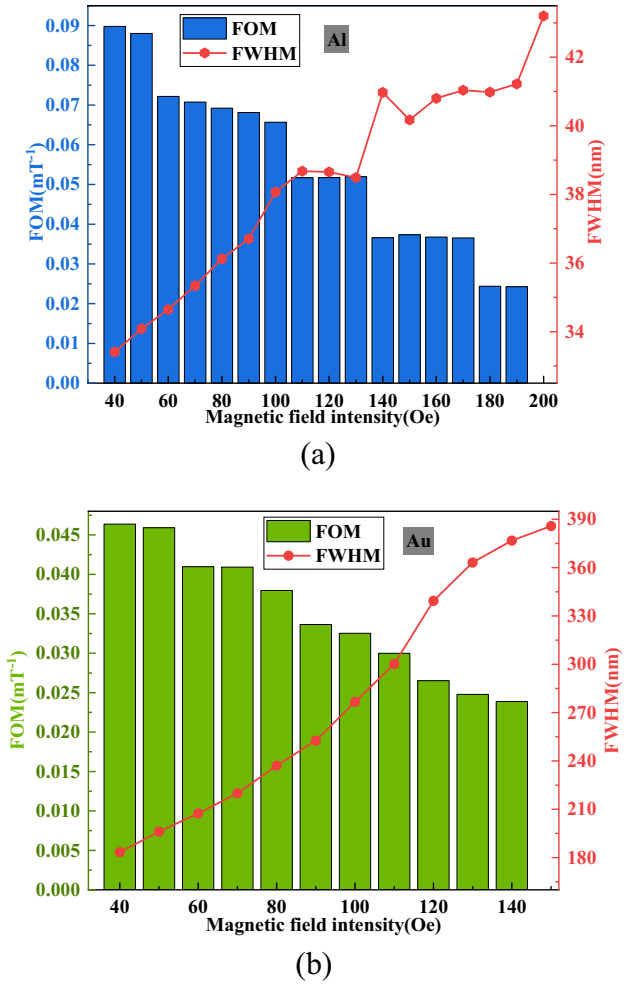

Fig. 9 FWHM and FOM for different magnetic fields: **a** SPR excited by Al and **b** SPR excited by Au

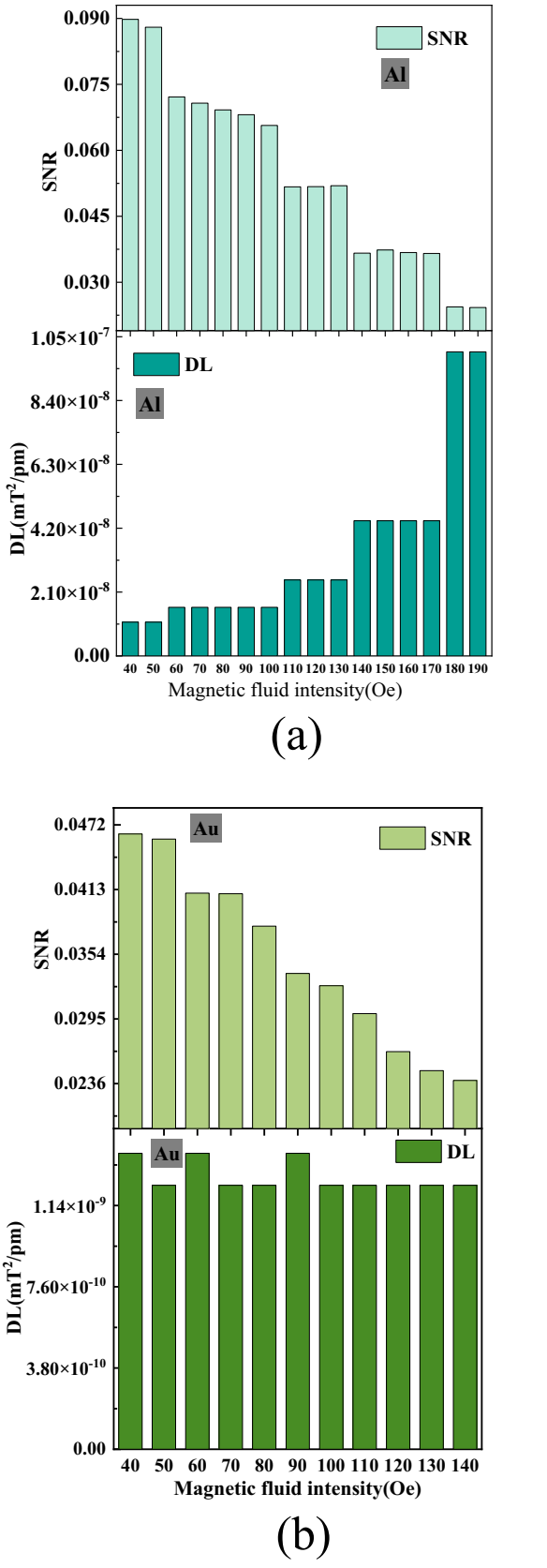

Fig. 10 SNR and DL: **a** sensors with Al-excited SPR; **b** sensors with Au-excited SPR

better. Figure 10a and b respectively describe the SNR and DL of the sensor when exciting SPR using Al and Au.

It is important to note that temperature impacts the refractive index of the MF [16], and its effect on the magnetic field sensitivity of the sensor is studied between 40 and 50 Oe. Figure 11a shows that as the temperature increases, the RW decreases linearly because the refractive index of MF decreases with increasing temperature, leading to a larger refractive index of the fundamental mode. As shown in Fig. 11b, the magnetic field sensitivity decreases as the temperature increases from 18.3 to 60.3 °C. In the temperature range between 18.3 and 30.3 °C, the magnetic field sensitivity remains constant at 8500 pm/mT. As the temperature rises from 35.3 to 40.3 °C, the magnetic field sensitivity decreases to 8000 pm/mT, showing a reduction of only 500 pm/mT. When the temperature increases to 45.3 °C, the magnetic field sensitivity decreases to 7500 pm/mT, and when the temperature rises from 50.3 to 60.3 °C, the magnetic field sensitivity decreases to 7000 pm/mT. Although

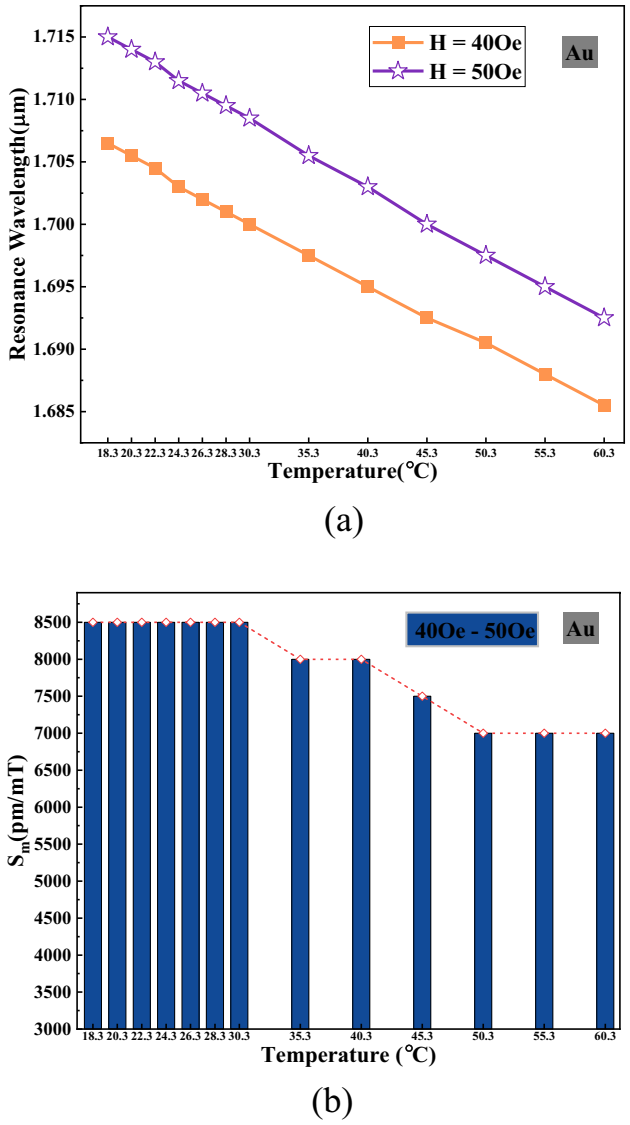

Fig. 11 **a** Resonance wavelength. **b** Magnetic field sensitivity at different temperatures

the magnetic field sensitivity decreases slightly when the temperature exceeds 30.3 °C, the decrease is minimal. Moreover, by implementing temperature compensation through a temperature control platform to maintain the temperature between 18.3 and 30.3 °C, the influence can be reduced. Therefore, the PCF-SPR magnetic field sensor maintains good magnetic field detection capabilities in spite of temperature variations.

To highlight the main advantages of this magnetic field sensor, Table 2 compares its performance with similar sensors reported recently.

Conclusion

An eccentric PCF-SPR magnetic field sensor with a micro-polished ring opening is designed. The sensor cladding contains air holes of only one size making it easy to manufacture. The properties of the magnetic field sensor with Au nanowires and Al nanowires for SPR excitation are studied. By placing metal nanowires inside the annular aperture, high sensitivity, high linearity, and a wide magnetic field detection range can be achieved. Based on the magnetic field sensitivity and FOM at 40 Oe, the structural parameters of the PCF-SPR magnetic field sensor are optimized. The effects of different metals and temperature on the sensing characteristics are analyzed and discussed. When SPR is excited by Al, the optimal structural parameters are $D = 3.6$ μm, $\lambda = 5.25$ μm, and $d = 0.4$ μm. In comparison, when Au is used to excite SPR, the optimal structural parameters were $D = 3.6$ μm, $\lambda = 5.25$ μm, and $d = 0.5$ μm. Numerical analysis shows that the magnetic field sensor using Al to excite SPR can detect magnetic fields in the range of 40 to 200 Oe, with a maximum magnetic field sensitivity of 3000 pm/mT. The sensor can detect a minimum magnetic field change of 3.33×10^{-5}mT, with an R^2 value of 0.99988, and when $H = 40$ Oe, FOM is 0.090 mT^{-1}. On the other hand, the magnetic field sensor using Au to excite SPR can detect magnetic fields in the range of 40 to 150Oe, with a maximum magnetic field sensitivity of 9000 pm/mT, a minimum magnetic field sensitivity of 8500 pm/mT, and an average magnetic field sensitivity of 8863.64 pm/mT. It can detect a minimum magnetic field change of 1.11×10^{-5} mT. The RW is fitted by a linear function with an R^2 of 0.99995. When $H = 40$ Oe, FOM is 0.046 mT^{-1}. The sensitivity and resolution of the magnetic field sensor using Au to excite SPR are outstanding. More

Table 2 Comparison of PCF-SPR sensor properties

Ref.	SPR Materials	Wavelength range (nm)	Magnetic field Range (Oe)	Sensitivity (pm/mT)	R^2	Resolution (mT)	Str. diagram
[8]	Au	700-780	25-200	779	0.9937	1.28×10^{-4}	
[9]	Au	1350-1470	50-130	650	/	1.54×10^{-4}	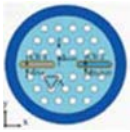
[10]	Au	850-1100	30-150	11500	0.98266	0.87×10^{-5}	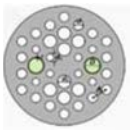
This work	Al Au	960-1160 1400-2100	40-200 40-150	3000 9000	0.99888 0.99995	3.33×10^{-5} 1.11×10^{-5}	

importantly, the RW demonstrates extremely high linearity, making it suitable for magnetic field detection. This PCF-SPR magnetic field sensor features a wide magnetic field detection range, high magnetic field sensitivity, and ultra-high linearity, making it highly promising in aerospace applications, early earthquake warning, and biomedical fields.

Author Contribution Xingdi Luo: Conceptualization, Methodology, Software, Writing-Original Draft. Jingwei Lv: Investigation, Validation. Wei Liu: Conceptualization, Writing-Reviewing and Editing. Chao Mi: Investigation. Jianxin Wang: Formal analysis. Xili Lu: Validation. Lin Yang: Conceptualization. Qiang Liu: Resources. Paul K. Chu: Project administration. Chao Liu: Resources, Writing- Reviewing and Editing. All the authors reviewed the manuscript.

Funding This work was jointly supported by the Heilongjiang Provincial Natural Science Foundation of China (JQ2023F001), National Natural Science Foundation of China (12304480), Local Universities Reformation and Development Personnel Training Supporting Project from Central Authorities, Natural Science Foundation of Heilongjiang Province (LH2021F007), China Postdoctoral Science Foundation-funded project (2020M670881), and City University of Hong Kong Strategic Research Grant (SRG) (7005505), as well as City University of Hong Kong Donation Research Grants (DON-RMG 9229021 and 9220061).

Data Availability No datasets were generated or analysed during the current study.

Declarations

Competing Interests The authors declare no competing interests.

References

1. Liu C, Liu W et al (2021) Overview of refractive index sensors comprising photonic crystal fibers based on the surface plasmon resonance effect. Chin Opt Lett 19(10):102202. https://doi.org/10.3788/col202119.102202
2. Liu W, Liu C, Wang J et al (2023) Surface plasmon resonance sensor composed of microstructured optical fibers for monitoring of external and internal environments in biological and environmental sensing. Resu Phys 47:106365. https://doi.org/10.1016/j.rinp.2023.106365
3. Wang J, Pei L et al (2020) Magnetic field and temperature dual-parameter sensor based on magnetic fluid materials filled photonic crystal fiber. Opt Express 28(2):1456–1471. https://doi.org/10.1364/oe.377116
4. Mihailovic P, Petricevic S (2021) Fiber optic sensors based on the Faraday effect. Sensors 21(19):6564. https://doi.org/10.3390/s21196564
5. Kim YG, Moon HS, Park KJ et al (2011) Generating and detecting torsional guided waves using magnetostrictive sensors of crossed coils. NDT & E International 44(2):145–151. https://doi.org/10.1016/j.ndteint.2010.11.006
6. Wang Y, Xu J, Ning T et al (2022) Research on fiber-optic magnetic field sensor based on surface plasmon resonance. Optik 251:168346. https://doi.org/10.1016/j.ijleo.2021.168346
7. Fu X, Wang Y, Ran R et al (2021) A multi-directional magnetic field sensor based on tapered few mode fiber and magnetic fluid. Optik 240:166817. https://doi.org/10.1016/j.ijleo.2021.166817
8. Wang JK, Ying Y, Gao ZJ et al (2021) Surface plasmon resonance (SPR) based temperature and magnetic field sensor in a dual-core D-shaped photonic crystal fiber (PCF). Instrum Sci Technol 50(3):271–287. https://doi.org/10.1080/10739149.2021.1994417
9. Wang D, Yi Z et al (2022) Two-channel photonic crystal fiber based on surface plasmon resonance for magnetic field and

temperature dual-parameter sensing. Phys Chem Chem Phys 24(35):21233–21241. https://doi.org/10.1039/d2cp02778j
10. Tang C, Yang D et al (2024) Design and optimization of hexagonal SPR-based photonic crystal fiber magnetic field sensor with magnetic fluid infiltration. Opt Quant Electron 56(1):88. https://doi.org/10.1007/s11082-023-05532-y
11. Hoque AMT, Islam A, Haider F et al (2022) Dual polarized surface plasmon resonance refractive index sensor via decentering propagation-controlled core sensor. Optics Continuum 1(7):1474–1488. https://doi.org/10.1364/OPTCON.460520
12. Huang H, Zhang Z et al (2020) A highly magnetic field sensitive photonic crystal fiber based on surface plasmon resonance. Sensors 20(18):5193. https://doi.org/10.3390/s20185193
13. Bilal MM, Lopez AS, Thottoli A (2023) Numerical analysis of solid-core photonic crystal fiber based on plasmonic materials for analyte refractive index sensing. Photonics MDPI 10(10):1070. https://doi.org/10.3390/photonics10101070
14. Fu H, Tang Z, Gao W et al (2024) Surface plasmon resonance temperature sensor based on the conjoined-tube hollow-core antiresonant fiber with ultra-high temperature sensitivity. JOSA B 41(4):950–961. https://doi.org/10.1364/josab.517575
15. Sharma AK, Gupta BD (2005) On the sensitivity and signal to noise ratio of a step-index fiber optic surface plasmon resonance sensor with bimetallic layers. Optics Communications 245(1–6):159–169. https://doi.org/10.1016/j.optcom.2004.10.013
16. Fu H, Guo Y, Gao W et al (2024) Ultra-high sensitivity weak magnetic field detecting magnetic fluid surface plasmon resonance sensor based on a single-hole fiber. Opt Express 32(9):15025–15040. https://doi.org/10.1364/oe.520047
17. Liu W, Shi Y, Yi Z et al (2021) Surface plasmon resonance chemical sensor composed of a microstructured optical fiber for the detection of an ultra-wide refractive index range and gas-liquid pollutants. Opt Express 29(25):40734–40747. https://doi.org/10.1364/oe.444323
18. Fan ZK, Fang SB, Li SG et al (2019) Refractive index sensor based on high-order surface plasmon resonance in gold nanofilm coated photonic crystal fiber. Chin Phys B 28(9):094209. https://doi.org/10.1088/1674-1056/ab327a
19. Liu C, Wang F, Zheng S et al (2016) Analysis of a highly birefringent asymmetric photonic crystal fibre based on a surface plasmon resonance sensor. J Mod Opt 63(12):1189–1195. https://doi.org/10.1080/09500340.2015.1135257
20. Rifat A, Mahdiraji G, Chow D et al (2015) Photonic crystal fiber-based surface plasmon resonance sensor with selective analyte channels and graphene-silver deposited core. Sensors 15(5):11499–11510. https://doi.org/10.3390/s150511499
21. Liu Y, Peng W (2020) Fiber-optic surface plasmon resonance sensors and biochemical applications: a review. J Lightwave Technol 39(12):3781–3791. https://doi.org/10.1109/jlt.2020.3045068
22. Tang YX, Zhang X, Zhu XS et al (2021) Dielectric layer thickness insensitive EVA/Ag-coated hollow fiber temperature sensor based on long-range surface plasmon resonance. Opt Express 29(1):368–376. https://doi.org/10.1364/oe.412805
23. Zhang S, Han B, Zhang Y et al (2022) Multichannel fiber optic SPR sensors: realization methods, application status, and future prospects. Laser Photonics Rev 16(8):2200009. https://doi.org/10.1002/lpor.202200009
24. Islam A, Haider F, Aoni RA et al (2021) U-grooved dual-channel plasmonic sensor for simultaneous multi-analyte detection. JOSA B 38(10):3055–3063. https://doi.org/10.1364/JOSAB.435255